Artificial chemical and magnetic structure at the domain walls of an epitaxial oxide

S. Farokhipoor, C. Magén, S. Venkatesan, J. Íñiguez, Christophe Daumont, D. Rubi, Etienne Snoeck, M. Mostovoy, C. de Graaf, A. Müller, et al.

LETTER

doi:10.1038/nature13918

Artificial chemical and magnetic structure at the domain walls of an epitaxial oxide

S. Farokhipoor[1]*, C. Magén[2,3]*, S. Venkatesan[4]†, J. Íñiguez[5], C. J. M. Daumont[1]†, D. Rubi[1]†, E. Snoeck[3,6], M. Mostovoy[1], C. de Graaf[1,7,8], A. Müller[4]†, M. Döblinger[4], C. Scheu[4]† & B. Noheda[1]

Progress in nanotechnology requires new approaches to materials synthesis that make it possible to control material functionality down to the smallest scales. An objective of materials research is to achieve enhanced control over the physical properties of materials such as ferromagnets[1], ferroelectrics[2] and superconductors[3]. In this context, complex oxides and inorganic perovskites are attractive because slight adjustments of their atomic structures can produce large physical responses and result in multiple functionalities[4,5]. In addition, these materials often contain ferroelastic domains[6]. The intrinsic symmetry breaking that takes place at the domain walls can induce properties absent from the domains themselves[7], such as magnetic or ferroelectric order and other functionalities, as well as coupling between them. Moreover, large domain wall densities create intense strain gradients, which can also affect the material's properties[8,9]. Here we show that, owing to large local stresses, domain walls can promote the formation of unusual phases. In this sense, the domain walls can function as nanoscale chemical reactors. We synthesize a two-dimensional ferromagnetic phase at the domain walls of the orthorhombic perovskite terbium manganite ($TbMnO_3$), which was grown in thin layers under epitaxial strain on strontium titanate ($SrTiO_3$) substrates. This phase is yet to be created by standard chemical routes. The density of the two-dimensional sheets can be tuned by changing the film thickness or the substrate lattice parameter (that is, the epitaxial strain), and the distance between sheets can be made as small as 5 nanometres in ultrathin films[10], such that the new phase at domain walls represents up to 25 per cent of the film volume. The general concept of using domain walls of epitaxial oxides to promote the formation of unusual phases may be applicable to other materials systems, thus giving access to new classes of nanoscale materials for applications in nanoelectronics and spintronics.

Oxide heteroepitaxy is a powerful strategy for strain engineering, because a very thin film grown epitaxially on a single-crystal substrate of slightly different lattice parameter can adopt the structure of the substrate. Because complex oxides are known to owe their physical responses to the subtle balance of several competing interactions, small modifications in the atomic distances can give rise to dramatic changes in the magnetic or electrical responses. Therefore, strained films can display physical properties very different from the bulk, and can even exhibit novel phases[11]. Apart from the horizontal interfaces created by growing one oxide on top of another, another type of interface can appear during epitaxial growth between two regions of the film with different crystal orientations. In some materials, these domain walls, or twin walls[12,13], have also shown higher conductivity than the contiguous domains[14,15].

Strained, (001)-oriented $TbMnO_3$ films have been grown on (001)-oriented $SrTiO_3$ substrates (refs 16–18 and Methods). Despite the large mismatch of 5% between the lattice parameters of the film and the substrate, the similarity between their in-plane lattice areas makes it possible for $TbMnO_3$ to be grown atomically flat and with high crystalline quality on single-crystal $SrTiO_3$ substrates, aided by the formation of crystallographic domains[10,17]. In $TbMnO_3$, as in most orthorhombic perovskites, the Tb atoms order in zigzag fashion along the [001] direction. Because of symmetry considerations, this zigzag ordering is mirrored at every domain wall of a [001]-oriented film. This produces a large difference in the bond distances at the domain walls, creating large strains highly localized in two-dimensional (2D) sheets at the walls. In epitaxially strained thin films, the average size of the domains depends on the magnitude of the strain and on the film thickness[10,19,20], making it possible to engineer different domain wall densities and to investigate the effect of the intense and largely localized stresses on the functional properties of the films.

The local structure and chemistry of the films was investigated using scanning transmission electron microscopy (STEM) techniques (Methods). Figure 1a shows a high-angle annular dark-field (HAADF) image of the cross-section of one of the films. Apart from the domain walls (observed as vertical lines in the image), the films do not present dislocations or interfacial layers, suggesting that domain formation is the main mechanism responsible for accommodating the epitaxial strain in the films. Geometrical phase analysis of the HAADF image[21] shows, along the whole film, a homogenous change in the unit-cell strain in the out-of-plane direction (ε_{zz}) of about −5% with respect to the substrate lattice parameter ($a_s = 0.390$ nm) (Fig. 1b). The strain in the in-plane direction (ε_{xx}) is also homogeneous within each domain, but at the domain walls there is 3% less strain than in the domain bulk (Fig. 1c). Figure 1d shows an atomically sharp TEM image of the same film taken in plane-view mode. Owing to the fourfold symmetry of the substrate, the domain walls tend to run along the two perpendicular in-plane directions. The domain wall structure and density coincide perfectly with those observed by the bright-field TEM image in Fig. 1e. For the thinnest films, the domains can be as small as 5 nm in the direction perpendicular to the walls[10]. The clear observation of the domain walls in the HAADF-STEM images as atomically sharp lines raises the question of their nature and the origin of this peculiar contrast.

Further insight into the nature of the walls is provided by a detailed analysis of the HAADF images in Fig. 2a, obtained on a 25 nm-thick $TbMnO_3$ film in the vicinity of the $SrTiO_3$ substrate. The domain walls exhibit columns with alternating contrast along the pseudo-cubic [001] direction. A detail of one of these walls, shown in Fig. 2b, enables the construction of a model representing the atomic structure of the wall and based on the Z contrast of the metal ions in the HAADF image and the crystal structure of bulk $TbMnO_3$ (Z, atomic number). Assisted by

[1]Zernike Institute for Advanced Materials, University of Groningen, 9747 AG Groningen, The Netherlands. [2]Laboratorio de Microscopías Avanzadas (LMA), Instituto de Nanociencia de Aragón (INA) - ARAID, and Departamento de Física de la Materia Condensada, Universidad de Zaragoza, 50018 Zaragoza, Spain. [3]Transpyrenean Advanced Laboratory for Electron Microscopy (TALEM), CEMES - INA, CNRS - Universidad de Zaragoza, 30155 Toulouse, France. [4]Department of Chemistry and CeNS, Ludwig-Maximilians-Universität München, Butenandtstrasse 5-11 (E), 81377 Munich, Germany. [5]Institut de Ciència de Materials de Barcelona (ICMAB-CSIC), Campus UAB, 08193 Bellaterra, Spain. [6]CEMES - CNRS, 30155 Toulouse, France. [7]Universitat Rovira i Virgili, 43007 Tarragona, Spain. [8]Institució Catalana de Recerca i Estudis Avançats (ICREA), 08010 Barcelona, Spain. †Present addresses: Max-Planck-Institut für Eisenforschung GmbH, 40237 Düsseldorf, Germany (S.V., A.M., C.S.); Groupe de Recherche en Matériaux, Microélectronique, Acoustique et Nanotechnologies (GREMAN, UMR7347), University of Tours, 37020 Tours, France (C.J.M.D.); Gerencia de Investigaciòn y Aplicaciones and Instituto de Nanociencias y Nanotecnologìa, CAC-CNEA, 1650 San Martín, Argentina (D.R.).
*These authors contributed equally to this work.

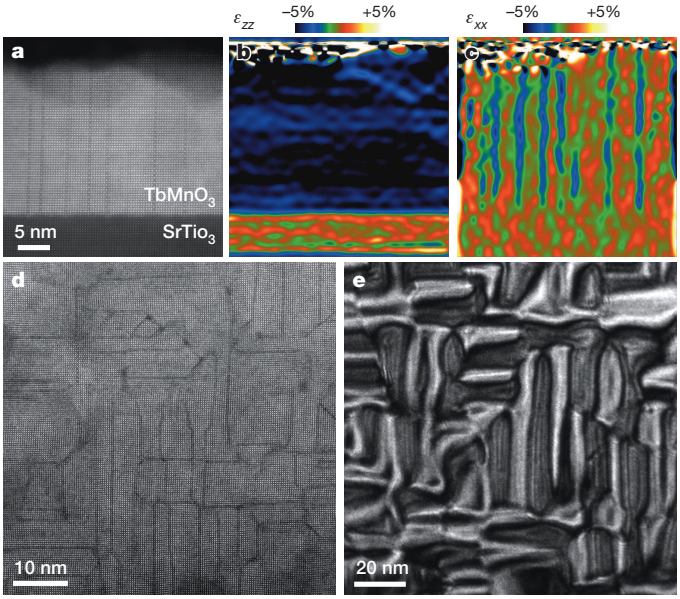

Figure 1 | Atomic-resolution domain structure of strained $TbMnO_3$. **a**, Cross-sectional HAADF-STEM image of a 25 nm-thick $TbMnO_3$ thin film grown on $SrTiO_3$. **b**, **c**, Components ε_{zz} (**b**) and ε_{xx} (**c**) of the strain tensor (colour scales), obtained by geometrical phase analysis of **a**. This shows that the domains grow uniformly strained, whereas stress is partly released at the domain walls. **d**, **e**, HAADF-STEM (**d**) and bright-field TEM (**e**) images of $TbMnO_3$ thin films with the same thickness in plane-view configuration, showing a coincident in-plane domain structure.

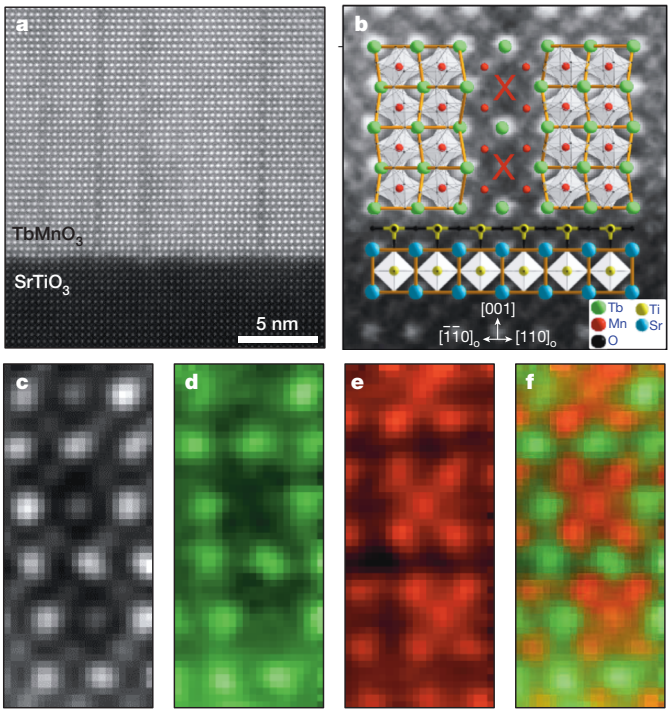

Figure 2 | Structure and chemistry of the domain walls. **a**, HAADF-STEM image of the $TbMnO_3$–$SrTiO_3$ interface. **b**, Detail of a domain wall close to the interface with the substrate, with the proposed atomic model superimposed. **c**–**f**, Spectrum image of the domain wall collected simultaneously with the HAADF signal (**c**): integrated intensities of the Tb $M_{4,5}$ (**d**) and Mn $L_{2,3}$ (**e**) edges from the spectrum image. **f**, Colour map composed using **d** and **e**, with the Mn signal in red and the Tb signal in green, showing the substitution of alternate Tb atoms for Mn to create a new 2D phase at the domain wall.

this model, a simple domain wall structure can be proposed on the basis of the alternation of fully Tb-occupied columns ('Tb columns') and Tb-deficient columns ('X columns') of A sites of the ABO_3 perovskite structure, which could be attributed either to Tb vacancies or to replacement of Tb by a lighter element. Though HAADF imaging suggests the existence of a reduced amount of Tb in the A sites of every other column of atoms at the domain walls, this technique cannot fully assess the chemical nature of the X columns. To that end, atomic-resolution chemical mapping has been carried out combining aberration corrected HAADF-STEM imaging and electron energy loss spectroscopy (Methods). This permits an unambiguous determination of the chemical composition of each atomic column. Figure 2c–f reveals that the X columns at the domain walls consist of Mn atoms substituting for Tb atoms. By comparison of the Mn signal from the X positions with that from regular Mn positions (outside the walls), it can be stated that Tb is replaced with Mn at almost all sites in most X columns. The same reasoning suggests that the Mn lattice at B sites of the wall apparently remains unperturbed with respect to the matrix, in such a way that the wall appears atomically thin from the crystallographic and chemical viewpoint. We claim that this chemical substitution of Tb by the smaller Mn cation takes place to avoid the presence of very close Tb–Tb atom pairs, which would occur in our domain walls as a result of the Tb zigzag ordering along the z direction (Fig. 2b). Indeed, the ordered Mn-for-Tb substitution releases the stress at the domain wall, as confirmed by Fig. 1c.

We now turn to investigate the physical properties of the newly synthesized phase. In $TbMnO_3$, the main magnetic interactions are ferromagnetic within each Mn (001) layer and antiferromagnetic between the layers[22]. It is then expected that the additional Mn atom present at the wall, placed between two antiferromagnetically interacting Mn planes, will experience magnetic frustration because it cannot be simultaneously aligned ferro- or antiferromagnetically with both neighbouring layers. This frustration leads to canting of spins, close to the walls, resulting in the appearance of a net magnetization. A net magnetic moment has been observed in epitaxially grown thin films of $TbMnO_3$ (refs 16, 18, 23, 24) and other orthorhombic manganites[25,26]. Various mechanisms have been put forward to explain this macroscopic magnetic response so distinct from that of the bulk material: strain-induced spin canting[18], interface magnetism[26], uncompensated spins at antiferromagnetic domain walls and magnetoelectric coupling at domain walls[12] have been reported. Solving the magnetic structure of a new Mn–O environment embedded in a crystal of $TbMnO_3$, which already has a complex magnetic structure, is a great challenge for which a holistic investigation, including theoretical calculations is needed. Here we present the first necessary steps in this direction.

The magnetic properties have been investigated using SQUID (superconducting quantum interference device) magnetometry. Figure 3a shows the magnetic susceptibility as a function of temperature measured on heating under field-cooling and zero-field-cooling conditions. The splitting between field cooling and zero field cooling that takes place below ~40 K (the bulk paramagnetic–antiferromagnetic transition temperature), as well as the shape of the inverse susceptibility curves deviating downwards with respect to the Curie behaviour (Methods), clearly point to the presence of a net magnetic moment in the films, which decreases with increasing film thickness. Figure 3b plots the in-plane component of the magnetization (M_{in}) versus magnetic field (H) measured at 10 K for films of different thicknesses. By zooming in around the low-field region (Fig. 3c), it can be seen that the remanent magnetization $M_{in}(H = 0)$ scales inversely with the film thickness, the same as the density of domain walls (or the inverse domain area), and is as large as 0.48 Bohr magnetons (μ_B) per formula unit (f.u.) for the 5 nm thin film and $0.11\,\mu_B$ f.u.$^{-1}$ for the 25 nm film (Fig. 3d).

We performed first-principles calculations to gain further atomistic insight into this novel structure at the domain walls of our $TbMnO_3$ films (Methods). We modelled the domain wall by considering the boundary between two ferroelastic domains that are rotated by 90° (about the out-of-plane [001] axis) with respect to each other[17], which allows us to reproduce the pattern of Tb displacements that is apparent in Fig. 2b.

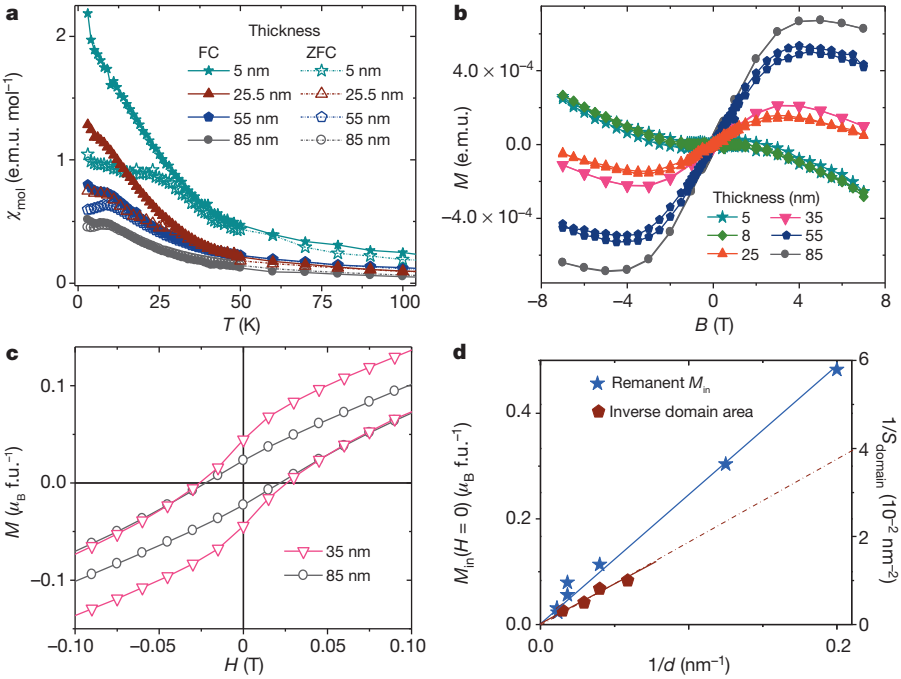

Figure 3 | Magnetic behaviour of the strained $TbMnO_3$ films. **a**, Field-cooled (FC) and zero-field-cooled (ZFC) magnetic susceptibilities as functions of temperature for various thicknesses. **b**, In-plane magnetization (M) versus magnetic field (H) at 10 K, for the films in **a**. **c**, Close-up of the low-field region of two of the curves in **b**, showing the remanent magnetization, $M_{in}(H = 0)$. The magnetization is normalized per formula unit of a hypothetical homogeneous $TbMnO_3$ film. **d**, $M_{in}(H = 0)$ versus the inverse of the film thickness. The inverse domain area (or density of domain walls) is also plotted using the data of ref. 10.

Additionally, we placed Mn atoms at alternating A sites in the boundary plane, also in accordance with our experimental findings. We then ran a structural relaxation of this initial structure, including a short simulated annealing to better search for the global energy minimum, and obtained the result depicted in Fig. 4. Interestingly, we find two different types of Mn atom occurring at the boundary planes. The first type (Mn(1) in the following) presents a tetrahedral coordination with four nearest-neighbouring oxygen atoms; in contrast, the second type (Mn(2)) displays a quasi-square-planar coordination with four nearest-neighbouring oxygens. This difference in local coordination is a consequence of the structural discontinuity, affecting the rotations of the O_6 octahedra, associated with our twin boundary. This gives rise to two crystallographically different A sites that alternate along the in-plane direction parallel to the wall (Fig. 4b, c).

As expected, the differently coordinated Mn atoms have distinctive properties. Our calculations indicate that Mn(1) atoms have an associated magnetic moment of about 4.5μ_B, which is considerably larger than that of the Mn atoms within the domains (about 3.7μ_B). This result suggests

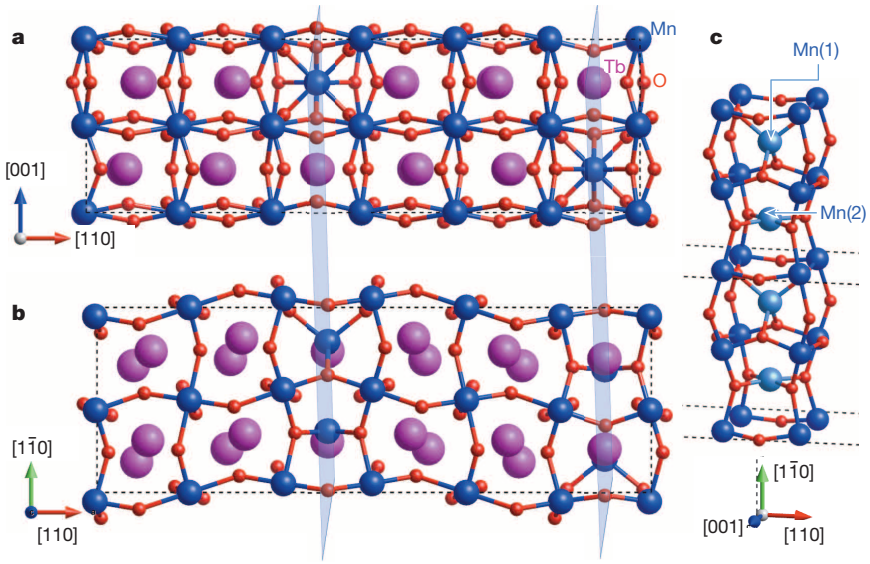

Figure 4 | Crystal structure of the new 2D phase. **a**, **b**, Lateral (**a**) and top (**b**) views of the DFT+U supercell, containing two domains and two domain wall planes (light blue). The A-site columns in which Tb is replaced by Mn are most clearly seen in **a**, showing the discontinuity in the zigzag Tb displacement pattern across the domain wall. Red, O; pink, Tb; dark blue, Mn in domains. **c**, Detail of one column of substitutional Mn cations (light blue) at the domain wall. The two distinct crystallographic A sites at the domain wall result from the patterns of oxygen octahedra rotations of the neighbouring domains. The spatial directions correspond to the orthorhombic setting. Light blue, Mn at domain walls.

that Mn(1) is less positively charged than the Mn cations within the domains. For Mn(2), we obtain a magnetic moment of about $3.8\mu_B$, which is much closer to the value obtained for the regular B-site Mn cations. We also computed the average magnetic interaction between the Mn atoms located in the domain wall and its neighbouring Mn cations. In addition, we did embedded cluster calculations to check the appropriateness of this approximation (Methods). To simplify the DFT+U calculation (density functional theory plus 'Hubbard U'; see Methods), we assumed a ferromagnetic arrangement of B-site Mn spins in our simulated supercell, and computed the energies associated with having different spin arrangements of Mn(1) and Mn(2). We obtained that, on average, Mn(1) interacts antiferromagnetically with its eight neighbouring Mn cations, the corresponding coupling constant being $J(1) \approx 1.61$ meV (we obtain 1.92 meV if no epitaxial constraints—that is, bulk-like conditions—are assumed in the simulation). In contrast, we obtain an average ferromagnetic interaction of $J(2) \approx -0.63$ meV for Mn(2) (-0.58 meV in bulk-like conditions). Finally, we find a small antiferromagnetic coupling, of about 0.08 meV (0.07 meV in bulk-like conditions) between neighbouring Mn(1) and Mn(2) atoms within the wall.

To understand the magnetic properties of this novel 2D phase, we used the exchange constants obtained from DFT+U calculations to simulate the magnetic ordering in the film (Methods). Figure 5 shows the minimum-energy configuration of Mn spins in two neighbouring domains and in the domain walls separating them (one unit cell thick), viewed from the [001] direction. The red and blue arrows respectively indicate the orientations of spins in the upper and lower Mn layers of the double unit cell in the domains, and the magenta arrows correspond to spins in the domain walls. Spins inside the domains show the A-type antiferromagnetic ordering (layers of parallel spins coupled antiferromagnetically along the [001] direction) rather than the spiral ordering found in bulk $TbMnO_3$ (ref. 27), because the compressive strain in the film relieves magnetic frustration[28] (Methods). Because the [100] and [010] axes in neighbouring domains are interchanged, spins form '90° antiferromagnetic domain walls', on either side of which the spin directions differ by 90°. As in the bulk material, the magnetization inside the domains cancels owing to the antiparallel arrangement of spins in neighbouring (001) layers. However, near each domain wall we find an uncompensated-for magnetic moment: the exchange coupling of a Mn ion in the wall to eight neighbouring spins at the domain edges favours parallel ordering of the latter spins, independently of whether this coupling is ferromagnetic or antiferromagnetic, thus inducing a large magnetic moment at the 'interface' between the domains and the wall equal to 10.16 μ_B per Mn spin in the wall. Because real samples show domain walls aligned in two perpendicular directions, approximately half of the domain walls will not contribute to the measured in-plane remanent magnetization. Therefore, according to the theoretical model, a magnetic moment of $\sim 5.1\mu_B$ per Mn spin in the wall, that is, $0.15\mu_B$ f.u.$^{-1}$, should be detected in our experiments (Methods). This is in very good agreement with the $\sim 0.10\mu_B$ f.u.$^{-1}$ found experimentally. A smaller experimental value is expected because domain wall pinning, domain dynamics and demagnetization fields are not taken into account by the model. The long-range magnetodipolar interactions will then favour parallel in-plane magnetic moments, that is, the ferromagnetic state.

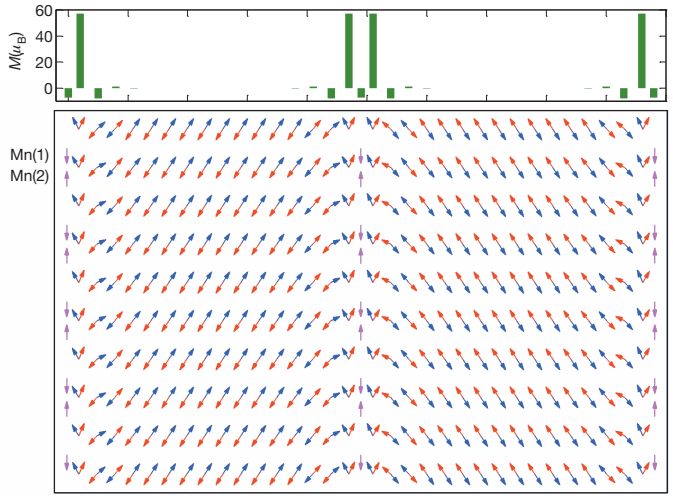

Figure 5 | Simulated magnetic order of the new 2D phase. The ordering of Mn spins in two neighbouring domains and the three associated domain walls viewed from the [001] direction (plane view) for a spin model with exchange parameters taken from DFT+U simulations (Methods). The domains are one unit cell thick and 16 unit cells wide. The red and blue arrows respectively indicate the orientations of spins in the upper and lower Mn layers in the domains, and the magenta arrows show the direction of spins in the domain walls. At the top is shown the net in-plane magnetic moment per atomic plane parallel to the domain wall.

We have described a route to synthesizing novel 2D phases by taking advantage of the large stresses present at crystallographic domain walls of epitaxially strained complex oxides. This approach should work in other epitaxial, [001]-oriented orthorhombic $A^{3+}B^{3+}O_3$ perovskites under compressive strain, especially in those containing multivalence B cations that offer higher flexibility for chemical interactions, and in those showing discontinuity in the tiltings of the oxygen octahedra at the domain walls. Moreover, the separation between the 2D sheets can be tuned, which makes them of potentially great interest in spintronic and electronic devices such as spin valves or magnetic storage media. We believe that this work opens a new route for the synthesis of diverse chemical environments in complex oxides.

Online Content Methods, along with any additional Extended Data display items and Source Data, are available in the online version of the paper; references unique to these sections appear only in the online paper.

Received 7 June; accepted 19 September 2014.

1. Lee, J. H. *et al.* A strong ferroelectric ferromagnet created by means of spin–lattice coupling. *Nature* **466,** 954–958 (2010).
2. Haeni, J. H. *et al.* Room-temperature ferroelectricity in strained $SrTiO_3$. *Nature* **430,** 758–761 (2004).
3. Llordés, A. *et al.* Nanoscale strain-induced pair suppression as a vortex-pinning mechanism in high-temperature superconductors. *Nature Mater.* **11,** 329–336 (2012).
4. Wang, J. *et al.* Epitaxial $BiFeO_3$ multiferroic thin film heterostructures. *Science* **299,** 1719–1722 (2003).
5. Choi, K. J. *et al.* Enhancement of ferroelectricity in strained $BaTiO_3$ thin films. *Science* **306,** 1005–1009 (2004).
6. Salje, E. K. H. Ferroelastic materials. *Annu. Rev. Mater. Res.* **42,** 265–283 (2012).
7. Daraktchiev, M., Catalan, G. & Scott, J. F. Landau theory of ferroelectric domain walls in magnetoelectrics. *Ferroelectrics* **375,** 122–131 (2008).
8. Catalan, G. *et al.* Flexoelectric rotation of polarization in ferroelectric thin films. *Nature Mater.* **10,** 963–967 (2011).
9. Lee, D. *et al.* Giant flexoelectric effect in ferroelectric epitaxial thin films. *Phys. Rev. Lett.* **107,** 057602 (2011).
10. Venkatesan, S., Daumont, D., Kooi, B. J., Noheda, B. & De Hosson, J. T. M. Nanoscale domain evolution in thin films of multiferroic $TbMnO_3$. *Phys. Rev. B* **80,** 214111 (2009).
11. Zubko, P., Gariglio, S., Gabay, M., Ghosez, P. & Triscone, J. M. Interface physics in complex oxide heterostructures. *Annu. Rev. Condens. Matter Phys.* **2,** 141–165 (2011).
12. Catalan, G., Seidel, J., Ramesh, R. & Scott, J. F. Domain wall nanoelectronics. *Rev. Mod. Phys.* **84,** 119–156 (2012).
13. Salje, E. K. H. Multiferroic domain boundaries as active memory devices: trajectories towards domain boundary engineering. *ChemPhysChem* **11,** 940–950 (2010).
14. Seidel, J. *et al.* Conduction at domain walls in oxide multiferroics. *Nature Mater.* **8,** 229–234 (2009).
15. Farokhipoor, S. & Noheda, B. Conduction through 71° domain walls in $BiFeO_3$. *Phys. Rev. Lett.* **107,** 127601 (2011).
16. Rubi, D. *et al.* Ferromagnetism and increased ionicity in epitaxially grown $TbMnO_3$ films. *Phys. Rev. B* **79,** 014416 (2009).
17. Daumont, C. J. M. *et al.* Epitaxial $TbMnO_3$ thin films on $SrTiO_3$ substrates: a structural study. *J. Phys. Condens. Matter* **21,** 182001 (2009).
18. Marti, X. *et al.* Emergence of ferromagnetism in antiferromagnetic $TbMnO_3$ by epitaxial strain. *Appl. Phys. Lett.* **96,** 222505 (2010).
19. Roitburd, A. L. Equilibrium structure of epitaxial layers. *Phys. Status Solidi A* **37,** 329–339 (1976).
20. Tagantsev, A. K., Cross, L. E. & Fousek, J. *Domains in Ferroic Crystals and Thin Films* 567–596 (Springer, 2010).

21. Hÿtch, M. J., Snoeck, E. & Kilaas, R. Quantitative measurement of displacement and strain fields from HREM micrographs. *Ultramicroscopy* **74,** 131–146 (1998).
22. Mochizuki, M. & Furukawa, N. Microscopic model and phase diagrams of the multiferroic perovskite manganites. *Phys. Rev. B* **80,** 134416 (2009).
23. Cui, Y., Wang, C. & Cao, B. $TbMnO_3$ epitaxial thin films by pulsed-laser deposition. *Solid State Commun.* **133,** 641–645 (2005).
24. Kirby, B. J. *et al.* Anomalous ferromagnetism in TbMnO3 thin films. *J. Appl. Phys.* **105,** 07D917 (2009).
25. Marti, X. *et al.* Strain-driven noncollinear magnetic ordering in orthorhombic epitaxial $YMnO_3$ thin films. *J. Appl. Phys.* **108,** 123917 (2010).
26. White, J. S. *et al.* Strain-induced ferromagnetism in antiferromagnetic $LuMnO_3$ thin films. *Phys. Rev. Lett.* **111,** 037201 (2013).
27. Goto, T., Kimura, T., Lawes, G., Ramirez, A. P. & Tokura, Y. Ferroelectricity and giant magnetocapacitance in perovskite rare-earth manganites. *Phys. Rev. Lett.* **92,** 257201 (2004).
28. Jiménez-Villacorta, F., Gallastegui, J. A., Fina, I., Marti, X. & Fontcuberta, J. Strain-driven transition from E-type to A-type magnetic order in $YMnO_3$ epitaxial films. *Phys. Rev. B* **86,** 024420 (2012).

Acknowledgements We are grateful to B. Kooi, T. Palstra, J. Fontcuberta, E. Canadell and the members of the Leverhulme Trust network 'International Network on Nanoscale Ferroelectrics', in particular J. F. Scott and F. Morrison, for discussions. This work is supported by NanoNextNL, a micro- and nanotechnology consortium of the Government of the Netherlands and 130 partners. It is also part of the research program NWO-Nano and is funded by the Foundation for Fundamental Research on Matter (FOM), which is financially supported by the Netherlands Organization for Scientific Research (NWO). C.M. and E.S. acknowledge the Laboratorio de Microscopias Avanzadas at Instituto de Nanociencia de Aragon, Universidad de Zaragoza, where the aberration-corrected TEM studies were conducted, and the support of the European Union under the Seventh Framework Programme under a contract for an Integrated Infrastructure Initiative Reference 312483-ESTEEM2. C.d.G. obtained financial support from the Spanish Administration (project CTQ2011-23140) and the Generalitat de Catalunya (project 2009SGR462). J.I. received financial support from MINECO-Spain (grants nos MAT2010-18113 and CSD2007-00041). D.R. is a fellow of CONICET. S.V., A.M., M.D. and C.S. acknowledge financial support from the German Science Foundation (DFG) via the Cluster of Excellence NIM. We made used of the facilities provided by the CESGA supercomputing centre.

Author Contributions C.J.M.D. and B.N. initiated the work. S.F. and C.J.M.D. grew the films and performed the structural and magnetic characterization. D.R. helped with the magnetic analysis. C.M. and E.S. performed the TEM measurements reported here. S.V., A.M., M.D. and C.S. performed preliminary TEM measurements and analysis that led to the discovery of the novel 2D phase. J.I. performed the density functional theory calculations. C.d.G. performed the embedded cluster calculations. M.M. simulated the magnetic structure. B.N., C.M., S.F., J.I. and M.M. wrote the paper. B.N. coordinated the activities. All authors discussed the results and commented on the manuscript.

Author Information Reprints and permissions information is available at www.nature.com/reprints. The authors declare competing financial interests: details are available in the online version. Readers are welcome to comment on the online version of the paper. Correspondence and requests for materials should be addressed to B.N. (b.noheda@rug.nl) or C.M. (cmagend@unizar.es).

METHODS

Growth and structural characterization of $TbMnO_3$ on $SrTiO_3$. $TbMnO_3$ has been intensively studied because of its multiferroic character and large magnetoelectric coupling[29–31]. Below 40 K, $TbMnO_3$ is antiferromagnetic with a sinusoidal spin order, which becomes a spiral order below 27 K. Bulk $TbMnO_3$ is an orthorhombic perovskite with space group *Pbnm* and lattice parameters $a = 5.2931$ Å, $b = 5.8384$ Å, $c = 7.4025$ Å. $SrTiO_3$ is cubic with lattice parameter $a = 3.905$ Å. The experiments were carried out on (001)-oriented $TbMnO_3$ films with thicknesses ranging from 5 to 85 nm directly grown on chemically and thermally treated (001)-oriented $SrTiO_3$ substrate by pulsed laser deposition. The base pressure of the vacuum system was of the order of 10^{-7} mbar and the oxygen pressure during growth was kept at 0.9 mbar. The substrate temperature during growth was 750 °C. A 248 nm-wavelength KrF excimer laser with a 2 J cm^{-2} energy density was focused on a $TbMnO_3$ stoichiometric pellet with a frequency of 0.5 Hz. The films were cooled down in an oxygen ambient pressure of 100 mbar with the cooling rate of 3 °C min^{-1} (ref. 17). The atomic force microscopy (AFM) investigation of the films showed atomically flat surfaces including one-unit-cell-high terraces that follow the ones present in $SrTiO_3$ substrate even up to 85 nm-thick films (Extended Data Fig. 1a).

The X-ray studies show the coherent growth of compressively strained $TbMnO_3$ along one of the two in-plane crystallographic directions of the $SrTiO_3$ substrate, as described in ref. 17. Despite the large lattice mismatch (+4.1% along [100] and −5.7% along [010]), because of the opposite signs of the strains along the two in-plane directions, the formation of orthorhombic domains allows the film to keep partial coherence with the substrate, either along the $[100]_c$ or the $[010]_c$ (substrate) directions. Importantly, it also determines the evolution of the lattice parameters with increasing thickness: the partial coherence with the substrate and the crystal twinning are able to keep the unit-cell in-plane area constant, and the out-of-plane lattice parameter and the unit-cell volume are thus basically unchanged for a large range of thicknesses from 5 to 85 nm (ref. 17). It can be argued that this is a very efficient way of minimizing the elastic energy of the system[10]. In fact, similar twinning patterns have been observed in $BiFeO_3$ films grown on $SrTiO_3$ (ref. 32).

Transmission electron microscopy. Plane-view and cross-sectional TEM specimens were prepared by tripod mechanical polishing and low-voltage Ar^+ ion milling for the final thinning. Domain wall density as a function of thickness was determined by bright-field imaging in a JEOL 2010, and preliminary STEM and electron energy loss spectroscopy (EELS) experiments (not shown here) were carried out in a non-corrected FEI Titan 80–300 microscope.

Aberration-corrected STEM analyses were carried out in a probe-corrected FEI Titan 60–300 microscope, fitted with a high-brightness field emission gun (X-FEG), a probe Cs corrector from CEOS and a Tridiem GIF Image Filter/Spectrometer 866 ERS from Gatan. Unless otherwise noted, the experiments were conducted at an acceleration voltage of 300 kV. Atomic-resolution *Z* contrast images were obtained by HAADF imaging in STEM. The convergence angle of 25 mrad yields a probe size below 1 Å. The inner and outer collection angles of the detector were 58 and 200 mrad, respectively. Aberration-corrected STEM was combined with EELS to obtain STEM-EELS spectrum images in the same probe-corrected FEI Titan 60–300. Atomic-resolution spectrum images were obtained with a probe size of ∼1 Å and a beam current of ∼ 400 pA. The average dwell time was 38 ms per pixel, the step between pixels was 0.4 Å, and an energy dispersion of 0.5 eV and an EELS collection angle of 87 mrad were used. High-energy-resolution STEM-EELS spectrum images to probe the electronic structure of the domain walls were obtained at 120 kV to minimize beam damage and increase inelastic scattering. In this case, the convergence angle was 22 mrad, the beam current was ∼350 pA, the dwell time was 38 ms per pixel, the step between pixels was 0.8 Å, and an energy dispersion of 0.2 eV and a collection angle of 74 mrad were used. Principal-component analysis was applied to the spectrum images to reduce background noise[33], and standard procedures for power-law background extrapolation and edge signal integration were followed.

Geometrical phase analysis of the HAADF images was carried out with the HREM Research software package to determine the strain of the $TbMnO_3$ thin film with respect to the substrate. The reference for the geometrical phase was always taken in the substrate; the frame of the image was avoided to minimize scan distortion effects. To reduce the influence of small sample instabilities during image acquisition, the strain components were extracted from two consecutive, 90°-rotated images and only the strain component along the fast scan direction was taken from each image.

The local Mn oxidation state was determined following a calibration for the position of the O K pre-peak with respect to the nominal oxidation state of the $La_xCa_{1-x}MnO_3$ series reported elsewhere[34]. The method consists of a two-Gaussian fit of the main peak and the pre-peak of the O K edge, of which the latter is related to the hybridization of O 2*p* and Mn 3*d* orbitals. The energy difference between the maxima is related to the oxidation state of Mn, and this method has been shown to be the most accurate for this purpose[34]. Considering that $TbMnO_3$ is isoelectronic with respect to $LaMnO_3$, the same calibration was used to estimate the deviation from the matrix oxidation state of our system. Crushed powder of the original $TbMnO_3$ target was analysed to determine the nominal oxidation state of Mn.

The EELS O K edge of a thin $TbMnO_3$ particle of the target and the Gaussian curves fitted are shown in Extended Data Fig. 2. Extended Data Fig. 3 illustrates the local determination of the Mn oxidation around the domain walls. The $TbMnO_3$ domains, that is, the regions far from the walls, present a nominal Mn oxidation state of about +3.2, which compares well with the Mn oxidation state of crushed powder from the target used to grow the films. This fact would agree with a tendency of the system to present areas strongly deficient in Tb, inducing a locally distorted lattice that would help to accommodate epitaxial strain. However, the oxidation state of a 1 nm-thick region around the Tb-deficient domain walls decreases down to +3. Thus, it is plausible that Mn in the X columns would be less positively charged (that is, +2 character), which would reduce the oxidation state of the defect to +3, assuming that the Mn in the B positions have the same valence as that measured in the domains. A fully quantitative determination of the oxidation state of Mn in each position around the defect has not been possible, as the Mn oxidation state maps are not atomic-resolution ones. Even in this case, a column-resolved accurate determination of such small variation of the Mn oxidation state would be doubtful owing to dechannelling and delocalization phenomena of inelastic scattering.

The variation of the Mn oxidation state was also monitored by measuring the distance between the Mn white lines, the L_2 and L_3 edges, as illustrated in Extended data Fig. 4. In this case, to the best of our knowledge there is no reference calibration compatible with our system and with the accuracy required. Thus, the result is qualitative, although the tendency is what is expected for the decrease of the Mn oxidation state, that is, an increment in the energy difference between the L_2 and L_3 lines[35].

Magnetic measurements. The magnetic behaviour of our $TbMnO_3$ thin films was studied with a Quantum Design MPMS-XL magnetometer based on a SQUID sensor. This magnetometer is equipped with a cryostat that can set temperatures between 1.9 and 400 K and magnetic fields up to 9 T. Before each measurement, the complete system was cooled down to liquid-helium temperature. The magnetization was then measured as a function of the temperature at a fixed field, or as a function of the magnetic field at a fixed temperature. The sensitivity of the SQUID is up to 10^{-8} e.m.u.

The measured magnetic signal includes the diamagnetic signal of the $SrTiO_3$ substrates (linear with the field) and the strong paramagnetic contribution of the Tb^{3+} ions (nonlinear with the field, following a Brillouin function). The latter makes it difficult to extract the Mn-related ferromagnetic saturation magnetization. Therefore, the best way to estimate the ferromagnetic component of the 2D phase is by measuring the remanent magnetization, $M(H = 0)$, where both the diamagnetic $SrTiO_3$ and paramagnetic Tb^{3+} contributions become negligible. Details about the magnetic units used to present the data can be found in the following.

Substrate contribution to the magnetic data. It has to be mentioned that, owing to the small $TbMnO_3$ volume present in our nanometric films, the measured magnetic signal was rather small and close to the sensitivity of the magnetometer. In addition, the paramagnetic signal of the Tb^{3+} is present in the magnetic response (the M–H curves were taken at 10 K above the ordering temperature of Tb^{3+}). The diamagnetic signal arising from the $SrTiO_3$ substrates is also included in the data shown in Fig. 3b, c, and is responsible for the negative slope of the M–H curves. To make sure that there is no contribution of the substrate in the observed remanent magnetization, we carefully measured the magnetic signal of the bare substrates before the film deposition by performing several control experiments under the same sequences as later used for the $TbMnO_3$ thin films. In Extended Data Fig. 5, we show the magnetic response of the bare substrates together with the same total measured magnetic response (including film and substrate) displayed in Fig. 3c. It shows that the remanent magnetization is not coming from impurities in the substrates.

Normalization of the magnetic data. The in-plane magnetization measured at 10 K in thin films with thicknesses ranging from 5 to 85 nm is shown in Fig. 3b. The data are presented in units of Bohr magnetons per formula unit (μ_B f.u.$^{-1}$) to provide some absolute values that are independent of the sample volume being measured. However, because our films consist of two different phases (domains and walls) with different magnetic responses, the normalization is not straightforward to interpret, and any choice made requires an explanation. In this case, we have chosen to normalize per formula unit of standard $TbMnO_3$, that is, to divide by the number of formula units (or Mn atoms) of a hypothetical homogeneous $TbMnO_3$ film of the same dimensions as our samples. This number is referred below as N_T.

Because the density of domain walls is known (Fig. 3d), it is possible to renormalize the observed magnetization as Bohr magnetons per wall Mn, to compare with the theoretical calculations. This is done as follows.

The domains simulated in Fig. 5 of the main text are 17 (simple perovskite) unit cells wide, which is around 6.8 nm. From the experimental observations (TEM plane-view images), the aspect ratio of the domains is estimated to be 3.5:1, and the domain area can thus be written as $S = 3.5 \times w^2$, where w is the distance between domain

walls (the domain width). This value of $S = 162\,\mathrm{nm}^2$ corresponds, according to Fig. 3d, to a film thickness of 29 nm and, thus, from the measured magnetization values of the same figure, to $M_{in} = 0.10\mu_B$ f.u.$^{-1}$

To compare this value with the theoretical calculations, we notice that the real samples have domain walls running along two perpendicular directions and that the in-plane field is applied approximately along one of the two in-plane directions. Thus, the predicted theoretical value for our experimental conditions would be ~0.5 times the $10.2\mu_B$ per wall Mn estimated by our model (see main text), that is, $5.1\mu_B$ per wall Mn. Because the domains are 17 f.u. wide and there is one Mn at the wall every other (simple perovskite) unit cell, the number of Mn atoms at the wall for this film thickness is $N_w = N_T/34$, and the remanent magnetization per formula unit is thus $M_{in}(H = 0) = 5.1\mu_B/34 = 0.15\mu_B$, which is in quite good agreement with the observed $0.10\mu_B$ f.u.$^{-1}$, taking into account the assumptions made (see details of the theoretical calculations in the following sections).

The predicted magnetic moment above $10\mu_B$ per Mn spin in the wall seems large. Note that such large values arise because, for each Mn ion at the domain walls, there are several Mn ions contributing to the magnetic moment, as can be seen in Fig. 5. More precisely, the magenta spins of the A-site Mn atoms that are at the centre of the wall cancel out among themselves; however, the spins of the B-site Mn cations near the wall contribute to the net magnetic moment, and add up to create a very large magnetization.

Additional magnetic measurements. In Extended Data Fig. 6, we display the out-of-plane magnetic M–H curves for the same samples, for which the diamagnetic signal of the substrate has been subtracted. No clear dependence on film thickness has been observed in this case.

In Extended Data Fig. 7, we plot the inverse susceptibility for the 55 nm film. The extrapolation of the high-temperature tail gives a negative Curie–Weiss temperature, reflecting the expected antiferromagnetic interaction present at regular $TbMnO_3$ within the domains. However, below 45–50 K the data deviates from the Curie–Weiss law towards larger susceptibility values, consistent with the appearance of a net magnetic moment.

DFT calculations. First-principles simulations were performed using the generalized gradient approximation to DFT as implemented in the code VASP[36,37]. More precisely, we used the generalized gradient approximation adapted to solids proposed in ref. 38, including a 'Hubbard *U*' correction with $U = 4$ eV and $J = 1$ eV for a better treatment of Mn 3*d* electrons[39]. The interactions between the ionic cores and the valence electrons were treated within the projector augmented-wave method[40], and the following electrons were explicitly considered in the simulations: O 2*s* and 2*p*; Mn 3*p*, 3*d* and 4*s*; Tb 5*p* and 6*s* (following a standard approximation, Tb is considered to have a 3+ valence, and its remaining 4*f* electrons are treated as core electrons). The electronic wavefunctions were represented in a plane-wave basis truncated at 400 eV. The simulation supercell used in most of the calculations consisted of a $6 \times 2 \times 2$ repetition of the elemental 5-atom perovskite cell, and the corresponding Brillouin zone integrations were performed in a $1 \times 2 \times 2$ grid of *k* points. These calculation conditions were checked to provide well-converged results. Additionally, our corrected DFT scheme was checked to render qualitatively and quasi-quantitatively accurate results for the description of the bulk orthorhombic phase of $TbMnO_3$. In particular, the leading magnetic interactions between Mn spins occurring in bulk $TbMnO_3$ were computed to be $J_{ab} = -0.32$ meV, $J_c = 0.53$ meV and $J_2 = 0.56$ meV, following the definitions in ref. 22. At a qualitative level, these values compare well with results in the literature (for example $J_{ab} = -0.79$ meV, $J_c = 1.26$ meV and $J_2 = 0.62$ meV, taken from ref. 22) and lead to the same type of ground-state spin arrangement. Obviously, a significant quantitative disagreement exists, which can be attributed to the different theoretical methods on which the respective calculations are based. We also considered a monodomain version of $TbMnO_3$ subject to the epitaxial strain that is typical of our films. In that case, we get $J_{ab} = -1.81$ meV, $J_c = 0.13$ meV and $J_2 = 0.56$ meV.

Embedded cluster calculations. In this work, embedded cluster calculations have been performed to check the DFT+*U* results on the average magnetic interactions between wall and bulk Mn atoms. Magnetic exchange energies have been calculated separately for all the pairs of Mn atoms that can be formed considering the wall Mn and its eight neighbours, using the DFT+*U* optimized structure as reference. The local nature of the magnetic exchange makes the cluster approach a natural starting point for studying this aspect of the electronic structure provided that an accurate representation of the material can be used in such a local approach. To this end, we defined a quantum region (the cluster) that consists of two neighbouring Mn^{3+} ions and the oxygen ions directly surrounding them. The electrons in this region were treated with standard *ab initio* wavefunction-based computational techniques capable of finding very good approximations to the eigenfunctions of the exact (non-relativistic) Hamiltonian. This cluster was embedded in a potential that accurately represents the electrostatic interaction of the cluster and the rest of the crystal. In the first place, the embedding takes care of the long-range Coulomb potential (that is, the Madelung potential) represented by placing point charges at a large number of sites around the cluster. To avoid an artificial delocalization of the cluster electron density to the point charges, a buffer between point charges and cluster was included in the embedding to represent the Coulomb and exchange interactions of the cluster electrons and the ions in the immediate surroundings of the cluster through model potentials[41]. The buffer region consists of eight Tb^{3+} and eleven Mn^{3+} potentials around the cluster. This modelling of the cluster very accurately reflects magnetic exchange between transition metal ions in oxides, as recently reviewed in ref. 42. The second essential ingredient for accurate estimates of the exchange parameter is the choice of the computational scheme to approximate the exact *N*-electron cluster wavefunction. In this work, we applied multiconfigurational second-order perturbation theory[43] (CASPT2) as implemented in the Molcas 7 program[44]. The active space used to construct the multiconfigurational zeroth-order wavefunction contains eight orbitals and eight electrons, corresponding to the four magnetic orbitals and unpaired electrons on each Mn^{3+} centre. The one-electron basis set has (6*s*, 5*p*, 4*d*, 2*f*, 1*g*) functions centred on Mn and (4*s*, 3*p*, 1*d*) functions on O (ref. 45). This computational scheme has been successfully applied to many different molecules and extended systems, including many different transition-metal oxides[46].

These calculations confirm the DFT+*U* result of a net antiferromagnetic coupling of the Mn(1) with the surrounding Mn ions. For the Mn(2), we find both antiferromagnetic and ferromagnetic interactions, with the former dominating over the latter. Hence, overall, the DFT+*U* calculations yield couplings with a stronger ferromagnetic character, a result that may be partly due to effects not captured by our embedded cluster calculations, for example the metallic nature of the domain boundaries in the DFT+*U* simulations.

Spin model of the domain wall array. A periodic array of structural domains was modelled by two domains of 16×10 pseudocubic unit cells each separated by domain walls with periodic boundary conditions in the direction normal to the walls and open boundary conditions in the transverse direction. We considered a classical spin model with the Hamiltonian

$$H_{spin} = \sum_{n,m} J_{nm} \mathbf{S}_n \bullet \mathbf{S}_m + \sum_n \left[K_c S_{nc}^2 + K_a S_{na}^2 \right]$$

where the first and the second terms respectively describe the exchange interactions and the single-ion anisotropies ($S = 2$). We used the exchange constants for $TbMnO_3$ films obtained from DFT+*U* calculations (see above), using bulk-like *J* values for the Mn atoms separated from the walls by not more than three lattice constants, because those regions seem to be relaxed in our experiments, and film-like *J* values for the rest of the Mn atoms in the domains. The ratio of the next-nearest-neighbour antiferromagnetic and nearest-neighbour ferromagnetic exchange constants, $|J_{ab}/J_a| \approx 0.31$, is smaller than the critical value of 1/2, above which the ferromagnetic ordering of spins in ab planes becomes frustrated. This is why spiral ordering that results in multiferroicity of bulk $TbMnO_3$ does not occur in films. Because the values of magnetic anisotropy parameters for films are unknown, we used $K_a = 0.165$ meV, deduced from inelastic neutron scattering experiments on lanthanum manganite[47], and assumed that $K_c > K_a$, which confines spins to the (001) plane. Mn spins in the walls have no in-plane anisotropy. The spin configuration minimizing H_{spin} was found using simulated annealing and numerical solution of the Landau–Lifshitz–Gilbert equation. The change in direction of the [100] and [010] axes at the domain walls forces the Mn spins to form perpendicular antiferromagnetic domain walls. The width of the antiferromagnetic domain walls increases with decreasing magnetic anisotropy, and so does the magnetic moment, which equals $\sim 28\mu_B$ per Mn spin in the wall for $K_a = 0.165$ meV and $\sim 35\mu_B$ for $K_a = 0$.

The magnetic moment of the wall is further enhanced by the polarization of Tb spins. We estimated the Tb magnetization by calculating the magneto-dipolar field induced by the Mn spin configuration shown in Fig. 5 on Tb sites, considering that Tb spins are Ising-like with an effective magnetic moment of $9.7\mu_B$. The Tb contribution to the domain wall moment, obtained by summing the moments of all Tb ions for a 5 nm-thick film at 10 K is about one-quarter of the calculated Mn contribution.

Novel 2D phase in perspective. Here we discuss the reasons why we think this 2D phase is novel.

(1) The most likely structural model that we have identified from first principles displays MnO_4 groups in a square-planar coordination, a configuration (almost) unheard of for manganese cations. Note that, from the point of view of coordination chemistry, one can argue that square planar arrangement will typically correspond to a d^8 (or maybe d^6) electronic configuration for the transition metal cation[48]. Some exceptions to this rule exist, but are extremely rare in the case of manganese. As far as we can tell, Mn in a quasi-square-planar coordination has been reported four times for molecules[49–52], and all those cases differ very clearly from the present case (diversity of ligands, significant asymmetry of the ligand fields and so on). For solid-state systems, we have not been able to find a single instance of square-planar MnO_4 group coordination. This strongly indicates that what we have in our domain walls

is a unique configuration made possible by the particular structural mismatch occurring at them.

(2) Most perovskite oxides display phases characterized by 'simple' patterns of rotations of their O_6 octahedra. Such patterns are simple in the sense that they do not involve a significant deformation of the O_6 groups and can be described using the well-known notation due to Glazer[53]. The few exceptions to this rule (for example in $NaNbO_3$ or some $BiFeO_3$ polymorphs[54–56]) tend to involve a complex rotation pattern about one of the main perovskite axes. At any rate, the situation in all those cases is very different from the abrupt discontinuity in the pattern of O_6 rotations that we have in our $TbMnO_3$ domain walls, which constitute a high-energy configuration stabilized by the epitaxial stress. To the best of our knowledge, such an O_6 rotation pattern is not found in any extended phase. Compared with the domain walls in other ferroelastic perovskites, what makes our present case unique is the ordered chemical substitution that occurs as a further stress-relief mechanism.

(3) We may think of our new material as a perovskite with a partial chemical substitution on the A site, with formula $(Tb_{1-x},Mn_x)MnO_3$. We are not aware of any extended phase, with this kind of chemical formula, in which the A-site species order in columns as we find they do in our domain walls.

One needs to be cautious in defining the specific chemical formula and structure of this novel phase. The corresponding three-dimensional phase would result from defining a basic unit around the domain wall, and the thickness of such a basic unit would determine the chemical formula. Furthermore, the way such units are repeated in space would need to be assumed to determine the space group and other basic structural features. There is no unique choice for either of those two issues. The actual facts about the novel phase are that, first, it is a ternary oxide with formula $(Tb_{1-x},Mn_x)MnO_3$. Assuming that the new three-dimensional crystal is defined exclusively by the structure at the domain wall plane, we would have $x = 0.5$ (that is $TbMn_3O_6$); if we include the neighbouring planes then $x = 1/6$, and so on for other values of x. Second, the multidomain configurations considered in our simulations have an approximately orthorhombic symmetry; hence, that would be the tentative assignment for the crystal system of this new phase.

Nevertheless, a three-dimensional phase with the features present at our domain walls, and stable at normal conditions, is highly improbable. Our domain wall structure presents distortions that are very unusual and high in energy for a perovskite lattice, and their occurrence in the absence of very peculiar stress constraints seems very unlikely.

29. Alonso, J. A., Martinez-Lope, M. J., Casais, M. T. & Fernandez-Diaz, M. T. Evolution of the Jahn-Teller distortion of MnO_6 octahedra in $RMnO_3$ perovskites (R = Pr, Nd, Dy, Tb, Ho, Er, Y): a neutron diffraction study. *Inorg. Chem.* **39,** 917–923 (2000).
30. Kimura, T. *et al.* Magnetic control of ferroelectric polarization. *Nature* **426,** 55–58 (2003).
31. Mostovoy, M. Ferroelectricity in spiral magnets. *Phys. Rev. Lett.* **96,** 067601 (2006).
32. Daumont, C. J. M. *et al.* Tuning the atomic and domain structure of epitaxial films of multiferroic $BiFeO_3$. *Phys. Rev. B* **81,** 144115 (2010).
33. Watanabe, M., Okunishi, E. & Ishizuka, K. Analysis of spectrum-imaging datasets in atomic-resolution electron microscopy. *Microscopy Anal.* **23,** 5–7 (2009).
34. Varela, M. *et al.* Atomic-resolution imaging of oxidation states in manganites. *Phys. Rev. B* **79,** 085117 (2009).
35. Schmid, H. K. & Mader, W. Oxidation states of Mn and Fe in various compound oxide systems. *Micron* **37,** 426–432 (2006).
36. Kresse, G. & Furthmuller, J. Efficient iterative schemes for ab initio total-energy calculations using a plane-wave basis set. *Phys. Rev. B* **54,** 11169 (1996).
37. Kresse, G. & Joubert, D. From ultrasoft pseudopotentials to the projector augmented-wave method. *Phys. Rev. B* **59,** 1758 (1999).
38. Perdew, J. P. *et al.* Restoring the density-gradient expansion for exchange in solids and surfaces. *Phys. Rev. Lett.* **100,** 136406 (2008).
39. Liechtenstein, A. I., Anisimov, V. I. & Zaane, J. Density-functional theory and strong interactions: orbital ordering in Mott-Hubbard insulators. *Phys. Rev. B* **52,** R5467 (1995).
40. Blöchl, P. E. Projector augmented-wave method. *Phys. Rev. B* **50,** 17953 (1994).
41. Barandiarán, Z. & Seijo, L. The ab initio model potential representation of the crystalline environment. Theoretical study of the local distortion in NaCl:Cu+. *J. Chem. Phys.* **89,** 5739 (1988).
42. Malrieu, J.-P., Caballol, R., Calzado, C. J., de Graaf, C. & Guihery, N. Magnetic interactions in molecules and highly correlated materials: physical content, analytical derivation, and rigorous extraction of magnetic Hamiltonians. *Chem. Rev.* **114,** 429–492 (2014).
43. Andersson, K. K. Malmqvist, P.-Å. & Roos, B. O. Second-order perturbation theory with a complete active space self-consistent field reference function. *J. Chem. Phys.* **96,** 1218–1226 (1992).
44. Aquilante, F. *et al.* MOLCAS 7: the next generation. *J. Comput. Chem.* **31,** 224–247 (2010).
45. Roos, B. O., Lindh, R., Malmqvist, P.-Å., Veryazov, V. & Widmark, P.-O. New relativistic ANO basis sets for transition metal atoms. *J. Phys. Chem. A* **109,** 6575–6579 (2005).
46. de Graaf, C., Sousa, C., de P. R. Moreira, I. & Illas, F. Multiconfigurational perturbation theory, an efficient tool to predict magnetic coupling parameters in biradicals, molecular complexes and ionic insulators. *J. Phys. Chem. A* **105,** 11371–11378 (2001).
47. Moussa, F. *et al.* Spin waves in the antiferromagnet perovskite $LaMnO_3$: a neutron-scattering study. *Phys. Rev. B* **54,** 15149 (1996).
48. Albright, T. A., Burdett, J. K. & Whangbo, M.-H. *Orbital Interactions in Chemistry* 295–298, 304–309 (Wiley, 1985).
49. Henkel, G., Greiwe, K. & Krebs, B. $[Mn(S_2C_6H_3Me)2]^{n-}$: mononuclear manganese complexes with square-planar (n = 1) and distorted tetrahedral (n = 2) sulphur coordination. *Angew. Chem. Int. Edn Engl.* **24,** 117 (1985).
50. Morris, R. J. & Girolami, G. S. Isolation and characterization of the first σ-organomanganese(III) complex. Crystal and molecular structure of (2,4,6-trimethylphenyl)dibromobis(trimethylphosphine)manganese(III). *Polyhedron* **7,** 2001 (1988).
51. Sellers, S. P., Korte, B. J., Fitzgerald, J. P., Reiff, W. M. & Yee, G. T. Canted ferromagnetism and other magnetic phenomena in square-planar, neutral manganese(II) and iron(II) octaethyltetraazaporphyrins. *J. Am. Chem. Soc.* **120,** 4662 (1998).
52. Salavati-Niasari, M. & Babazadeh-Arani, H. Cyclohexene oxidation with tert-butylhydroperoxide and hydrogen peroxide catalyzed by new square-planar manganese(II), cobalt(II), nickel(II) and copper(II) bis(2-mercaptoanil)benzil complexes supported on alumina. *J. Mol. Catal. Chem.* **274,** 58 (2007).
53. Glazer, A. M. The classification of tilted octahedra in perovskites. *Acta Crystallogr.* **B28,** 3384–3392 (1972).
54. Johnston, K. E. *et al.* The polar phase of $NaNbO_3$: a combined study by powder diffraction, solid-state NMR, and first-principles calculations. *J. Am. Chem. Soc.* **132,** 8732 (2010).
55. Prosandeev, S., Wang, D., Ren, W., Iñiguez, J. & Bellaiche, L. Novel nanoscale twinned phases in perovskite oxides. *Adv. Funct. Mater.* **23,** 234 (2013).
56. Wang, D., Salje, E. K. H., Mi, S.-B., Jia, C.-L. & Bellaiche, L. Multidomains made of different structural phases in multiferroic BiFeO3: a first-principles-based study. *Phys. Rev. B* **88,** 134107 (2013).

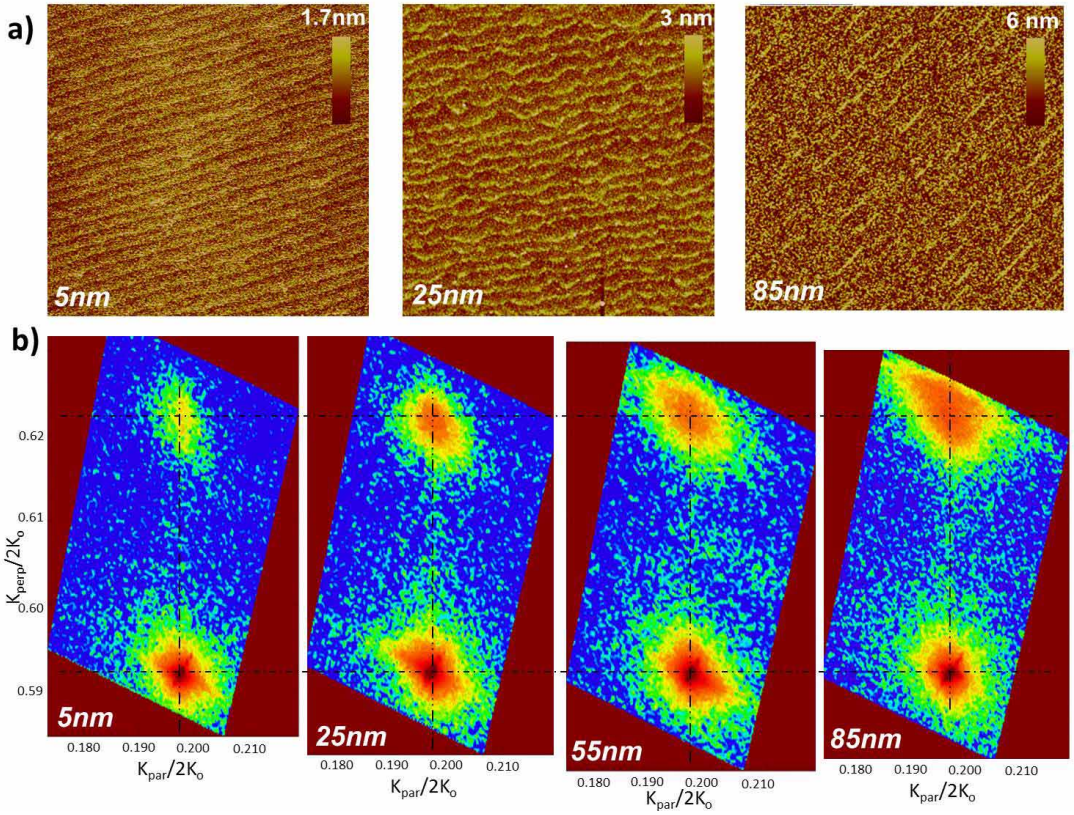

Extended Data Figure 1 | AFM and XRD characterization of the films. **a**, AFM images of the topography of $TbMnO_3$ films with three different thicknesses, showing flat surfaces and the presence of the substrate steps up to a thickness of 85 nm (film thickness is denoted in the left lower corner). **b**, XRD reciprocal-space maps around the substrate (103) reflection for four different thicknesses. The structural characterization of the films confirms the twin-domain configuration, constant out-of-plane lattice parameter and partial coherence with the substrate of the films used in this study, in agreement with those reported in ref. 17. The axes represent the components of the scattering wavevectors parallel (K_{par}) and perpendicular (K_{perp}) to the film surface in units of $2K_o = 4\pi/\lambda$, where λ is the X-ray wavelength.

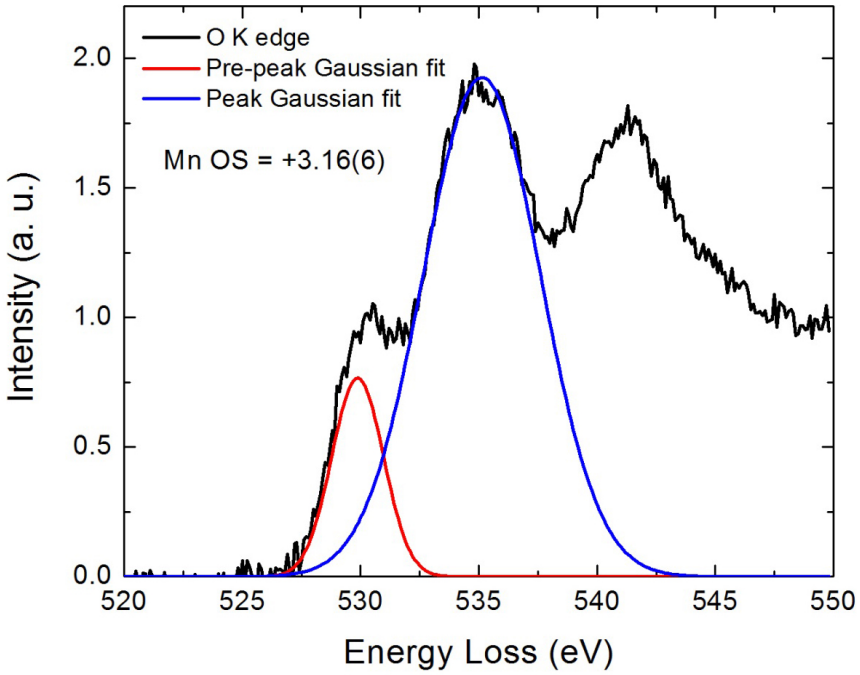

Extended Data Figure 2 | Reference EELS at the O K edge. Electron energy loss spectrum at the O K edge of crushed powder extracted from the $TbMnO_3$ target used to grow the sample studied in this work. This image includes the two Gaussian fits used to estimate the Mn oxidation state.

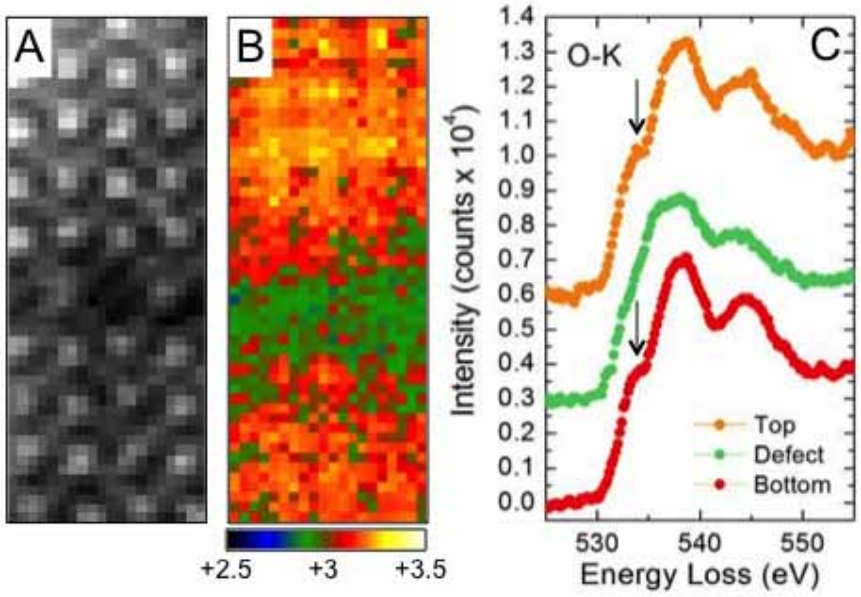

Extended Data Figure 3 | Domain wall EELS at the O K edge. Local determination of the Mn oxidation state from a spectrum image obtained around a $TbMnO_3$ domain wall following the analysis of the O K edge previously described. **a**, Simultaneously acquired HAADF signal. **b**, Mn oxidation state map. **c**, O K edges obtained by integrating spectra in the upper domain (orange), in the domain wall (green) and in the lower domain (red).

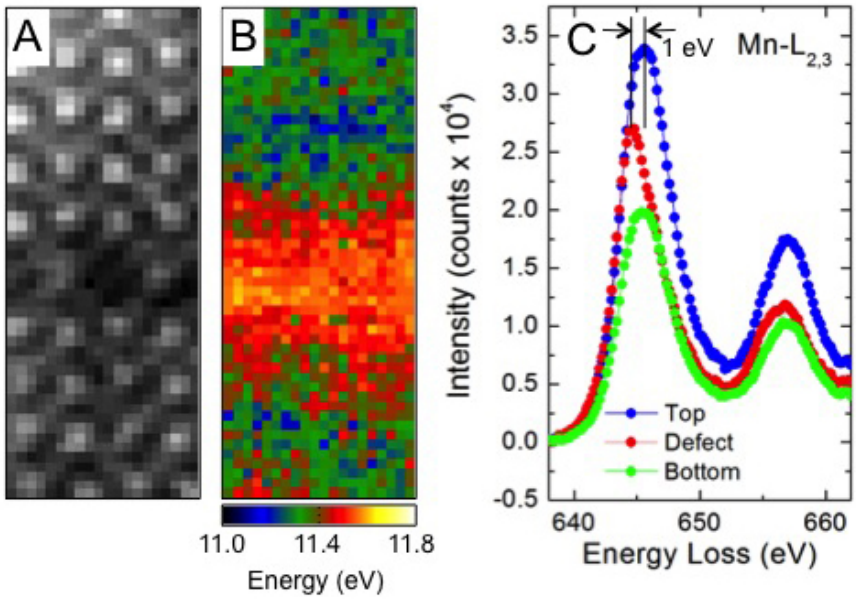

Extended Data Figure 4 | Domain wall EELS at the Mn $L_{2,3}$ edge. Map of the fine structure of the Mn $L_{2,3}$ edge around a $TbMnO_3$ domain wall, obtained from the spectrum image analysed in Extended Data Fig. 3. **a**, Simultaneously acquired HAADF signal. **b**, Energy difference between the maxima of the L_3 and L_2 peaks. **c**, Mn $L_{2,3}$ edges obtained by integrating spectra in the upper domain (blue), in the domain wall (red) and in the lower domain (green).

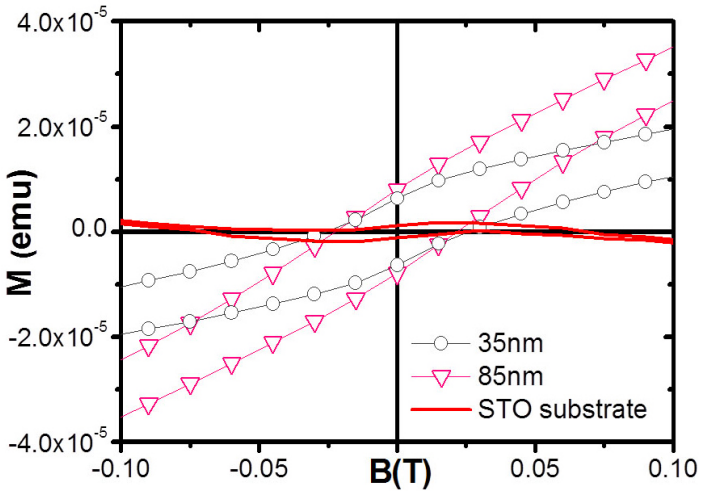

Extended Data Figure 5 | Substrate magnetic contribution. The M–H loop corresponding to the bare $SrTiO_3$ substrate is added to the curves in Fig. 3c, for direct comparison.

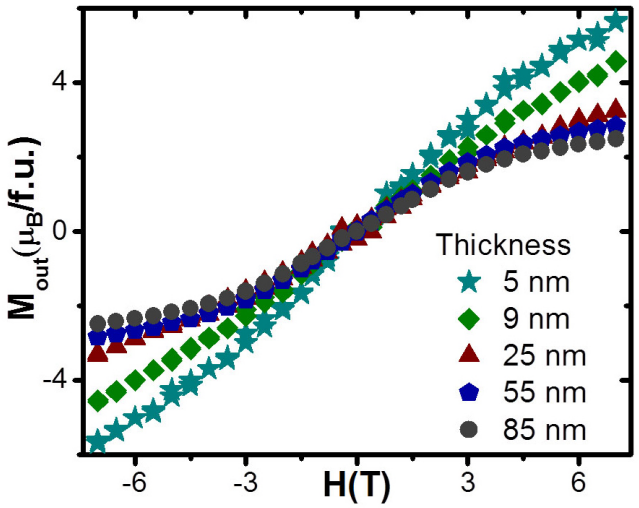

Extended Data Figure 6 | Out-of-plane magnetization. Out-of-plane magnetic M–H curves for the samples shown in Fig. 3b. The contribution of the substrate has been subtracted.

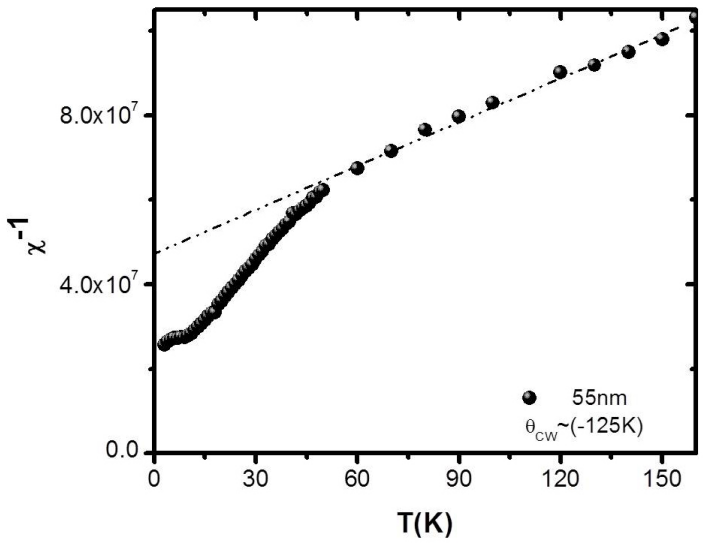

Extended Data Figure 7 | Inverse susceptibility. Inverse magnetic susceptibility of a 55 nm film showing deviation downwards from the Curie–Weiss law, which is indicative of the onset of a net magnetic moment below 45–50 K.